

## The quiescent double barrier regime in the DIII-D tokamak

E J Doyle<sup>1</sup>, L R Baylor<sup>2</sup>, K H Burrell<sup>3</sup>, T A Casper<sup>4</sup>, J C DeBoo<sup>2</sup>,  
D R Ernst<sup>5</sup>, A M Garofalo<sup>6</sup>, P Gohil<sup>3</sup>, C M Greenfield<sup>3</sup>, R J Groebner<sup>3</sup>,  
A W Hyatt<sup>3</sup>, G L Jackson<sup>3</sup>, T C Jernigan<sup>2</sup>, J E Kinsey<sup>7</sup>, L L Lao<sup>3</sup>,  
C J Lasnier<sup>4</sup>, J-N Leboeuf<sup>8</sup>, M Makowski<sup>4</sup>, G R McKee<sup>9</sup>, R A Moyer<sup>10</sup>,  
M Murakami<sup>2</sup>, T H Osborne<sup>3</sup>, W A Peebles<sup>1</sup>, M Porkolab<sup>11</sup>, G D Porter<sup>4</sup>,  
T L Rhodes<sup>1</sup>, J C Rost<sup>11</sup>, D Rudakov<sup>10</sup>, G M Staebler<sup>3</sup>, B W Stallard<sup>4</sup>,  
E J Strait<sup>3</sup>, R D Sydora<sup>12</sup>, E J Synakowski<sup>5</sup>, M R Wade<sup>2</sup>, G Wang<sup>1</sup>,  
J G Watkins<sup>13</sup>, W P West<sup>3</sup>, and L Zeng<sup>1</sup>

<sup>1</sup> Department of Electrical Engineering and PSTI, University of California, Los Angeles, CA 90095, USA

<sup>2</sup> Oak Ridge National Laboratory, Oak Ridge, TN 37381, USA

<sup>3</sup> General Atomics, P O Box 85608, San Diego, CA 92186, USA

<sup>4</sup> Lawrence Livermore National Laboratory, Livermore, CA 94550, USA

<sup>5</sup> Princeton Plasma Physics Laboratory, Princeton, NJ 08543, USA

<sup>6</sup> Columbia University, New York, NY 10027, USA

<sup>7</sup> Lehigh University, Bethlehem, PA 18015, USA

<sup>8</sup> Physics Department, University of California, Los Angeles, CA 90095, USA

<sup>9</sup> University of Wisconsin-Madison, Madison, WI 53706, USA

<sup>10</sup> University of California, San Diego, CA 92697, USA

<sup>11</sup> Massachusetts Institute of Technology, Cambridge, MA 02139, USA

<sup>12</sup> University of Alberta, Edmonton, Alberta, Canada

<sup>13</sup> Sandia National Laboratories, Albuquerque, NM 87185, USA

Received 22 June 2001

Published 22 November 2001

Online at [stacks.iop.org/PPCF/43/A95](http://stacks.iop.org/PPCF/43/A95)

### Abstract

Experiments on the DIII-D tokamak have identified a new sustained high-performance operating mode, termed the quiescent double barrier (QDB) regime. The QDB regime combines internal transport barriers (ITBs) with a quiescent, edge localized mode (ELM)-free H-mode edge, termed QH-mode, giving rise to separate core and edge transport barriers. These double barriers have been maintained for  $>3.5$  s ( $\sim 25\tau_E$ ), demonstrating a long-pulse, quasi-steady-state capability. The combination of core ITBs and edge H-mode temperature pedestals results in high-performance plasmas; a  $\beta_N H_{89}$  product of 7 has been maintained for  $10\tau_E$ , other peak (non-simultaneous) parameters include  $T_i \leq 17$  keV,  $\beta_N \leq 2.9\%$  m TMA<sup>-1</sup>,  $H_{89} \leq 2.6$ ,  $\beta \leq 3.8\%$ ,  $\tau_E \leq 160$  ms, and DD neutron rate  $S_n \leq 5.5 \times 10^{15}$  s<sup>-1</sup>. These results address a major issue with tokamak plasmas: how to sustain long-pulse, high-performance H-mode plasmas without ELMs, yet retaining the density and impurity control hitherto provided by ELMs. In these QDB plasmas ELMs are replaced by continuous benign MHD activity in the edge, which enhances particle transport.

A signature of operation with a QH-mode edge appears to be very large radial electric fields in the edge and scrape-off layer (SOL). In the core, simulations and modelling replicate many of the features of the observed transport and fluctuation behaviour, including the ion temperature profile and turbulence correlation lengths. Slow high-Z impurity accumulation ( $\tau \geq 500$  ms) is observed in the centre of many QDB plasmas, and is the subject of ongoing analysis. To date the QDB regime has only been obtained in plasmas with counter-NBI (injection anti-parallel to the plasma current), and with divertor cryopumping to control the density.

## 1. Introduction

Next-step devices are anticipated to operate in the high confinement mode (H-mode), with edge localized modes (ELMs) for density, radiated power, and impurity control [1]. However, ELMing H-mode plasmas have some non-optimal features, including the following: (1) Pulsed divertor heat and particle loads can lead to rapid erosion of the divertor plates [2]. (2) Type I (giant) ELMs can inhibit or destroy the internal transport barriers (ITBs) desired for advanced tokamak (AT) operation. (3) ELMs can couple to core MHD modes, and hence reduce the beta limit [3]. ITBs (regions of reduced transport relative to L-mode) are also desirable in next-step devices; ITBs at large radii can improve fusion performance and stability limits, and result in favourable bootstrap alignment with the total current profile [4]. The results reported here demonstrate that sustained, high-performance ELM-free H-mode plasmas are possible with good density and radiated power control. The results also demonstrate that the quiescent, ELM-free edge can easily be combined with core ITBs to obtain the benefits of both core and edge transport barriers.

The new quiescent double barrier (QDB) regime on DIII-D combines core transport barriers with a quiescent, ELM-free H-mode edge, termed QH-mode, giving rise to separate (double) core and edge transport barriers [4–6]. The combination of core ITBs and edge H-mode temperature pedestals results in improved performance relative to ITBs with an L-mode edge, or conventional ELMing H-mode. A  $\beta_N H_{89}$  product of 7 has been achieved for  $10\tau_E$  with QDB operation, substantially superior to ‘standard’ H-mode levels of  $\leq 4$ –5 ( $\beta_N H_{89}$  is a figure of merit for AT machines, where  $\beta_N = \beta/(I/aB_\phi)$  and  $H_{89} = \tau_E/\tau_{89}$ , where  $\tau_{89}$  is a global confinement scaling expression for L-mode plasmas [7]). QDB operation has been sustained for  $>3.5$  s ( $\sim 25\tau_E$ ), demonstrating a long-pulse, quasi-steady-state capability. Simulations and modelling replicate many of the features of the observed core transport and fluctuation behaviour, including the ion temperature profile and turbulence correlation lengths.

The work reported here stems from efforts on DIII-D to control and optimize internal transport barriers [4, 8]. The combined H-mode edge and core transport barriers in QDB plasmas result in broadened profiles and improved stability compared with an ITB alone. Previous attempts on DIII-D to combine ITBs with ELMing H-mode edges did not yield high-quality ITBs [9]. Specifically, ELM penetration to the core limited ITB development [9], while operation with a conventional ELM-free edge led to a steadily increasing and destabilizing edge pressure gradient [10]. Double barriers in the form of ITBs plus an ELMing H-mode edge have been obtained previously on larger devices such as JT-60U [11, 12], where the greater physical separation between the edge pedestal and the ITBs helps, and on JET in a regime with small ELMs [13]. A feature of the QDB regime on DIII-D is that the edge and core transport barriers are compatible and do not merge or negatively impact one another.

The remainder of this paper is structured as follows. An overview of QDB operation is presented in section 2, while the following sections consider in more detail the physics of the QH-mode edge (section 3), and issues associated with core aspects of QDB operation, such as transport and fluctuation behaviour (section 4). A summary is presented in section 5. Several new acronyms are introduced in this paper, which are summarized here: QDB—quiescent double barrier; QH-mode—quiescent H-mode; EHO—edge harmonic oscillation.

## 2. Overview of QDB operation

In this section we present an overview of operation in the QDB regime. An example of the time evolution of a QDB plasma is shown in figure 1. This discharge has  $I_p = -1.3$  MA (i.e. reversed current, so as to obtain counter-NBI) and  $B_T = 2.0$  T. The plasma makes a transition to H-mode shortly after counter-NBI heating is applied at 0.8 s. After an initial ELMing phase the discharge evolves into a quiescent phase (QH-mode), as marked by the disappearance of bursts on the  $D_\alpha$  emission. During this quiescent phase the line average density and radiated power become essentially constant, indicating that edge particle transport is sufficiently large for divertor cryopumping to control the density and low- $Z$  impurity content. Also during the QH-mode phase, a continuous oscillation is shown on magnetic probe signals after the ELMs cease, figure 1(f). This is the EHO, which will be discussed later in section 3.3. This discharge remains ELM free with a quiescent H-mode edge for over 3.5 s, or about  $25\tau_E$ , limited only by the duration of the NBI heating sources.

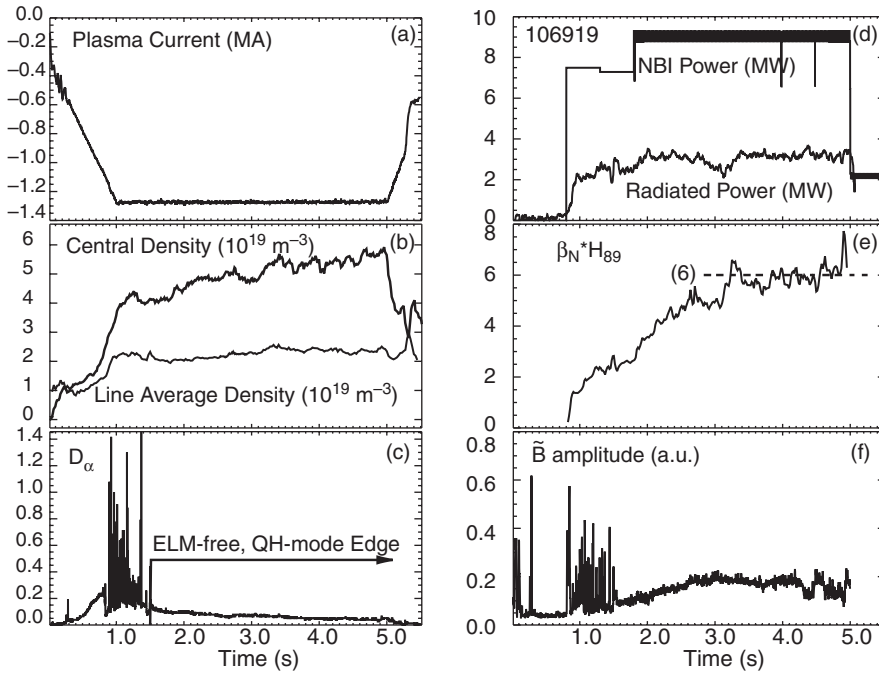


**Figure 1.** Example of the time history of a QDB plasma, 106919, showing (a) plasma current, (b) central and line average electron density, (c) divertor  $D_\alpha$  emission, (d)  $P_{\text{NBI}}$  and total radiated power, (e)  $\beta_N H_{89}$  (the  $H$ -factor is corrected for prompt ion orbit losses), and (f) frequency integrated amplitude of magnetic probe signal. The period of quiescent QDB/QH-mode operation is indicated in (c).

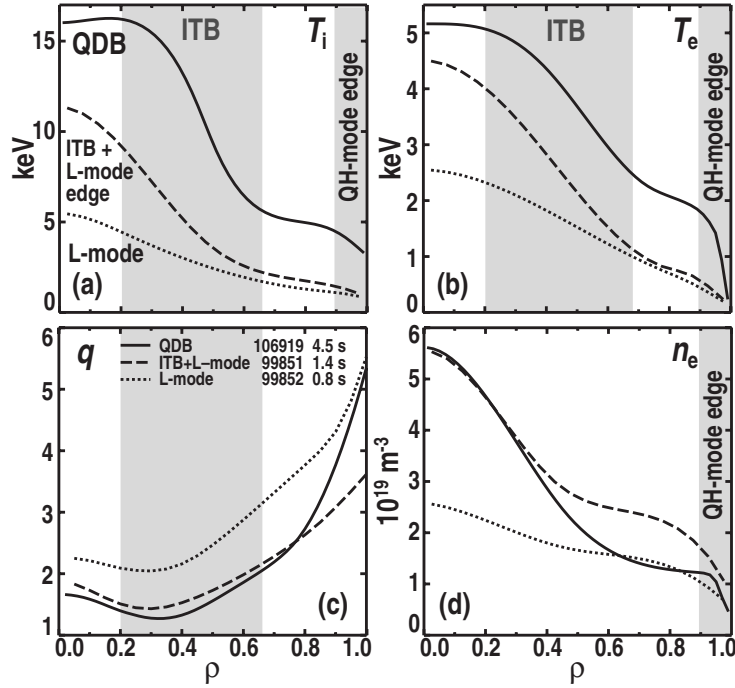


**Figure 2.** Profiles of (a)  $T_i$ , (b)  $T_e$ , (c)  $q$ , and (d)  $n_e$ , for three discharges. One is the QDB discharge illustrated in figure 1 (106919, solid curves), the second is a counter injection ITB discharge with an L-mode edge (99851, dashed curves), and the third is an L-mode discharge (99852, dotted curves). The double transport barrier in the QDB plasma is immediately apparent in the temperature profiles (shaded regions), with  $T_i(0)$  reaching 16 keV. From (c) it can be seen that the foot of the core transport barriers lies substantially outside  $\rho_{q_{min}}$ , while the typical low QDB edge densities can be seen in (d).

An ITB forms during the QH-mode period of the discharge shown in figure 1, resulting in improved core performance and creating a QDB plasma.  $\beta_N H_{89}$  rises continuously throughout the discharge to  $\sim 6\% \text{ m T MA}^{-1}$ , figure 1(e). The edge and core barriers obtained with QDB operation are clearly seen in the temperature profiles shown in figure 2. For comparison, profiles are also shown from a counter-NBI ITB discharge with an L-mode edge and a standard L-mode plasma. The QH-mode edge results in broader profiles with improved MHD stability compared with an ITB alone. The improved stability properties are demonstrated by the long-pulse capability of the QDB regime, and global stability to low order  $n = 1-2$  ideal ballooning modes has been confirmed by modelling. That QDB plasmas can have significant central density peaking is shown in figure 2(d). The  $q$  profile, figure 2(c), is moderately reversed (NCS operation), and the foot of the core transport barrier lies substantially outside  $\rho_{q_{min}}$ .

The QH-mode edge is obtained with counter-NBI at power levels down to  $\sim 2.5 \text{ MW}$  (at low current), and with divertor pumping to reduce and control the density. Addition of a core ITB inside the QH-mode edge to form a QDB plasma is straightforward using standard ITB formation techniques [8, 14] and higher heating powers ( $P_{\text{NBI}} \geq 7 \text{ MW}$ , though there is no sharp threshold). The QH-mode edge is characterized by continuous benign MHD activity, which usually takes the form of an EHO, visible on magnetic, density, and temperature fluctuation measurements. As discussed in section 3.3, particle transport associated with the EHO appears

to be responsible for the ability to maintain density and radiated power control in the ELM-free QH-mode regime. Another signature of QH-mode operation discussed in the same subsection is that there appear to be very large radial electric fields in the edge and scrape-off layer (SOL) during QH-mode.

With regard to the core ITBs, the observed transport and fluctuation behaviour is in reasonable agreement with modelling and simulations. As discussed in section 4.2, the core ion temperature profile has been replicated based on the regulation of turbulent transport by  $E \times B$  shear, while initial gyrokinetic modelling of ITG turbulence replicates the measured core turbulence correlation lengths. However, the observation of neoclassical ion transport with finite turbulence levels requires further measurements and modelling. In addition, measurements indicate that the core and edge transport barriers in QDB plasmas are separated by a region of low  $E \times B$  flow shear. An issue still under study is slow ( $\tau \geq 500$  ms) high- $Z$  impurity accumulation in the plasma centre, which is often observed in these QDB plasmas.

### 3. The QH-mode edge

The key element in obtaining a QDB discharge is to create a quiescent, ELM-free H-mode edge (QH-mode). In this section we discuss the experimental requirements for obtaining QH-mode, edge and divertor conditions during QH-mode operation, MHD oscillations associated with QH-mode operation, and possible ELM stabilization mechanisms.

#### 3.1. Operational conditions required to obtain QH-mode

The operational conditions required to access QH-mode can be summarized as follows:

1. Counter-NBI (injection anti-parallel to the plasma current), at power levels down to  $\sim 2.5$  MW (at low current). As discussed further in section 3.2, counter-NBI has different edge ion orbits as compared with co-NBI.
2. Divertor cryopumping to control the density, coupled with low line average densities of  $\sim 2\text{--}3 \times 10^{19} \text{ m}^{-3}$ . Typically, the only external particle fuelling to QH-mode discharges during current flat-top is that provided by the NBI. An upper density limit for QH-mode operation has yet to be determined, though it is known that moderate-to-large external gas puffs lead to a return to standard ELMing H-mode. The edge density has been raised transiently by 50% or more using a variety of techniques, including increasing the plasma triangularity [6], edge impurity injection and off-axis pellet injection. Further experiments are required to determine if higher edge densities can be sustained.
3. A larger than usual gap between the plasma edge and the outer wall (low-field side) of  $\sim 10$  cm. Again this is probably related to the different edge ion orbits associated with counter-NBI, and a larger outer gap is required to prevent ions from interacting with the wall.

QH-mode has been obtained in both upper and lower single-null discharges and across the following parameter range:  $0.67 \leq I_p \text{ (MA)} \leq 1.6$ ,  $0.95 \leq B_T \text{ (T)} \leq 2.1$ , triangularity  $\delta$  (of the side opposite the active X-point) of 0.16–0.7 and  $q$  of 3.7–4.6. Most work has been performed at  $1.2 \leq I_p \text{ (MA)} \leq 1.6$ ,  $1.8 \leq B_T \text{ (T)} \leq 2.1$ , and  $\delta \sim 0.4$ . In addition, QH-mode has been obtained with both orientations of  $B$  with respect to the divertor X-point. To date, QH-mode has only been observed to evolve from standard ELMing or ELM-free H-mode operation, i.e. we have yet to observe a direct transition from L-mode to QH-mode. Consequently, the input power required to obtain QH-mode operation has always been at or above that required for

standard H-mode operation. Systematic studies of the QH-mode power threshold have yet to be performed.

### 3.2. Edge and divertor conditions during QH-mode operation

Edge pedestal conditions during both the quiescent and ELMing phases of a single discharge are shown in figure 3. As can be seen, the edge gradients are similar or higher in the quiescent phase as compared with the ELMing phase, demonstrating that the quiescent phase is indeed a true H-mode regime. QH-mode also has other standard H-mode signatures, including an edge  $E_r$  well with high  $E \times B$  shear, an associated zone of reduced turbulence, and improved confinement. Also notable in figure 3 are the low pedestal density and high pedestal temperatures, particularly for ions, which can reach  $\sim 7$  keV.

Figure 4 shows a comparison of edge pedestal conditions in QH-mode with those in the Type I and Type III ELMing regimes. From figure 4(a) it can be seen that the QH-mode occurs at low normalized pedestal densities and high temperatures. The points from the ELMing phases of QH-mode discharges support the conclusion from figure 3 that the edge electron pedestal conditions are unchanged from the ELMing to quiescent phases of these discharges. Whether the ELMs in the pre QH-mode phase are low-density Type III ELMs is still under study. That the edge pressure gradient in QH-mode is at or above the ideal ballooning mode limit is shown in figure 4(b), though the edge gradient is less than for Type I ELMs. As the pressure limit was calculated using twice the electron pressure gradient, the data shown

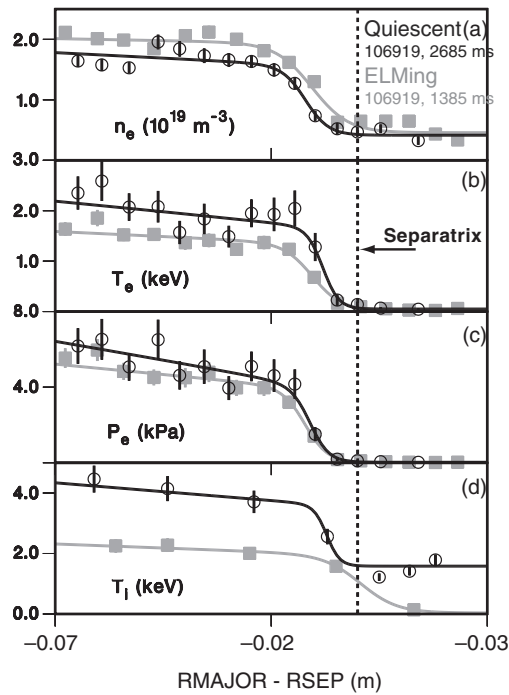


**Figure 3.** Profiles of (a)  $n_e$ , (b)  $T_e$ , (c)  $P_e$ , and (d)  $T_i$  in the edge pedestal region of discharge 106919, from both the ELMing (filled square symbols, grey curves) and QH-mode phases (open circles, black curves). The edge gradients are the same or higher in the QH-mode phase as compared with the ELMing phase.

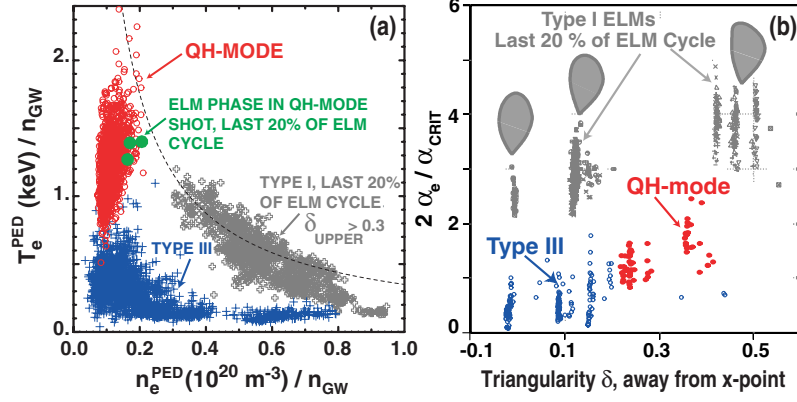


**Figure 4.** Comparison of edge pedestal conditions in QH-mode and Type I and III ELMing regimes. (a) The temperature at the top of the pedestal,  $T_e^{\text{PED}}$  versus  $n_e^{\text{PED}}$ , both quantities being determined from Thomson scattering data. Both axes are normalized by the Greenwald density,  $n_{\text{GW}}$ . The dashed curve illustrates a surface of constant pressure. (b) Maximum edge pressure gradient  $2\alpha_e$ , normalized to the ideal ballooning mode critical gradient, versus the triangularity  $\delta$  away from the X-point.  $\alpha$  is the normalized pressure gradient (ballooning parameter),  $\alpha = -q^2 R_0 \nabla \beta$ , where  $R_0$  is the mean major radius.

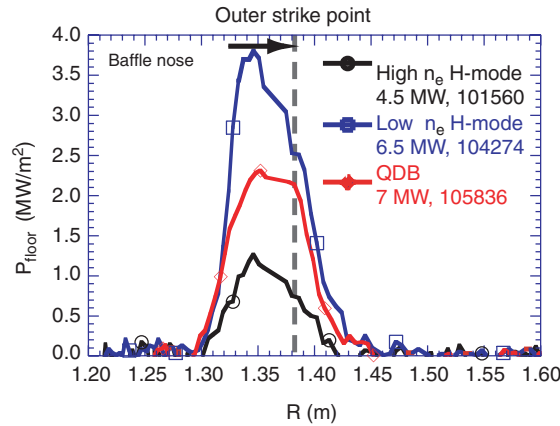


**Figure 5.** Comparison of the heat flux to the outer divertor strike-point for three discharges: a high-density ELMing H-mode ( $\bar{n}_e = 8 \times 10^{19} \text{ m}^{-3}$ ,  $P_{\text{NBI}} = 4.5 \text{ MW}$ , 101560, black curve), a low-density ELMing H-mode ( $\bar{n}_e = 3.6 \times 10^{19} \text{ m}^{-3}$ ,  $P_{\text{NBI}} = 6.25 \text{ MW}$ , 104274, blue curve), and a QDB discharge ( $\bar{n}_e = 2 \times 10^{19} \text{ m}^{-3}$ ,  $P_{\text{NBI}} = 7 \text{ MW}$ , 105836, red curve).

here may underestimate the edge pressure because of the substantial edge ion temperatures previously referred to. These data also show that the QH-mode edge pressure gradient increases with triangularity, as in standard ELMing H-mode [15]. These observations are consistent with an extensive body of prior work on ELM stability on DIII-D, which suggests that the edge stability limit may be set by kink/ballooning modes, and considerations of second stability access [15].

The low QH-mode edge densities and high temperatures result in a sheath-limited, collisionless edge, raising concerns about divertor heat flux loading. Surprisingly, the conducted heat flux remains relatively modest. Figure 5 shows a comparison of the heat

flux to the outer divertor strike-point, as determined from IR camera data, for a conventional high density H-mode plasma ( $\bar{n}_e = 8 \times 10^{19} \text{ m}^{-3}$ ,  $P_{\text{NBI}} = 4.5 \text{ MW}$ ), a low-density H-mode plasma ( $\bar{n}_e = 3.6 \times 10^{19} \text{ m}^{-3}$ ,  $P_{\text{NBI}} = 6.25 \text{ MW}$ ), and a QDB plasma ( $\bar{n}_e = 2 \times 10^{19} \text{ m}^{-3}$ ,  $P_{\text{NBI}} = 7 \text{ MW}$ ). As can be seen, the divertor strike-point heat flux is actually lower for the QDB plasma as compared with the low-density H-mode case and, allowing for the difference in input power, only  $\sim 30\%$  higher than the high-density conventional H-mode case. In addition, and in contrast to conventional ELMing H-mode, pulsed heat loads to the divertor are completely absent with QH-mode operation. However, during QH-mode operation the divertor heat load distribution is different than usual, with a large amount of power being deposited away from the strike-points. The higher than usual heat flux associated with the open outer midplane field lines may be due to the large SOL ion temperatures mentioned above, see figure 3(d). On a more general level it should be noted that present-day devices can match anticipated core or edge reactor conditions, but not both simultaneously [1]. It follows, therefore, that present-day devices with reactor relevant cores, such as the QDB plasmas presented here, may have non-optimal divertor conditions.

There is one significant difference in edge conditions observed between QH-mode operation and conventional ELM-free or ELMing H-mode. As can be seen from charge exchange recombination (CER)-derived measurements of the edge radial electric field,  $E_r$ , shown in figure 6(a), the QH-mode has a several times deeper  $E_r$  well inside the separatrix than a conventional co-NBI discharge at comparable power. In addition,  $E_r$  on the open field lines in the SOL outside the separatrix is also much higher. That the SOL plasma during QH-mode operation has  $E_r$  values usually associated with the H-mode edge transport barrier has been confirmed by data from a reciprocating Langmuir probe at the vessel midplane, figure 6(b). That these high  $E_r$  values in the SOL are directly associated with QH-mode operation, and not with H-mode operation with counter-NBI, is shown by Langmuir probe data from a conventional ELMing counter-NBI discharge, also shown in figure 6(b), indicating normal minimal  $E_r$  values in the SOL.

Counter-NBI is associated with a larger prompt ion loss, and a larger fraction of confined ion orbits which cross the separatrix than co-NBI discharges. This can be seen as follows: with respect to the location of ionization, counter-NBI ion orbits move outwards, while with co-NBI they move inwards. Ions crossing the separatrix should make the electric field inside

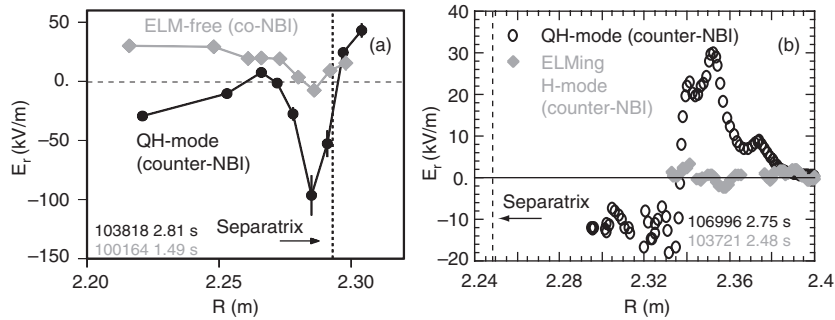


**Figure 6.** (a) Comparison of the edge radial electric field  $E_r$ , as determined from CER measurements, in a QH-mode discharge (103818, filled circle symbols, black curve) and a conventional ELM-free co-NBI discharge (100164, diamond symbols, grey curve) at comparable input power. (b) Comparison of the SOL  $E_r$ , as determined from Langmuir probe measurements, in a QH-mode discharge (106996, black open circle symbols) and in an ELMing counter-NBI discharge (103721, filled grey diamond symbols).

the separatrix more negative and the field outside more positive, as observed. In addition, the opposite toroidal plasma rotation direction with counter-NBI, as compared with co-NBI, should also result in a more negative  $E_r$  well inside the separatrix, such that both rotation and pressure gradient effects produce negative contributions to  $E_r$ . Negative shear in  $E_r$ , which occurs inside the separatrix, is such as to cause main ion orbit squeezing, while positive shear in  $E_r$ , which occurs in parts of the SOL in QH-mode, is such as to cause orbit expansion [16]. Thus, operation with counter-NBI should lead to a deeper, more negative  $E_r$  well inside the separatrix and a more positive SOL  $E_r$ , which should lead in turn to orbit expansion in the SOL. However, as already mentioned, the Langmuir probe data shown in figure 6(b) indicate that the increased  $E_r$  in the SOL is associated with QH-mode operation, and not counter-NBI *per se*.

The hypothesis that ions near the outer plasma midplane play a role in the creation of the large radial fields observed in QH-mode is supported by Langmuir probe measurements on the plasma bottom (away from the X-point in an upper single-null plasma), showing a much smaller  $E_r$  in the SOL. In addition, the data presented earlier in figure 3(d) show that  $T_i$  is  $\sim 1$  keV in the SOL, again consistent with enhanced ion effects in that region.

### 3.3. The EHO and enhanced particle transport

In most cases, QH-mode plasmas are associated with the presence of an EHO. The EHO is continuous during QH-mode operation and is visible on magnetic, density, and temperature fluctuation measurements. As its name implies, the EHO typically has multiple harmonics, with toroidal mode numbers ranging from 1 to 10. The harmonic content can vary both from shot to shot and over time within a single discharge. An example of the frequency spectrum of an EHO as measured by a magnetic probe is shown in figure 7. In this particular example  $n = 1-4$  components are evident at first, changing to a single, stronger  $n = 3$  component later in time. As yet, the specific instability mechanism responsible for the EHO has not been identified. A summary of the characteristics of the EHO and a comparison to the quasi-coherent mode responsible for the ELM-free EDA H-mode regime on C-MOD [17] is shown in table 1. From these characteristics it is evident that while both the EHO and the quasi-

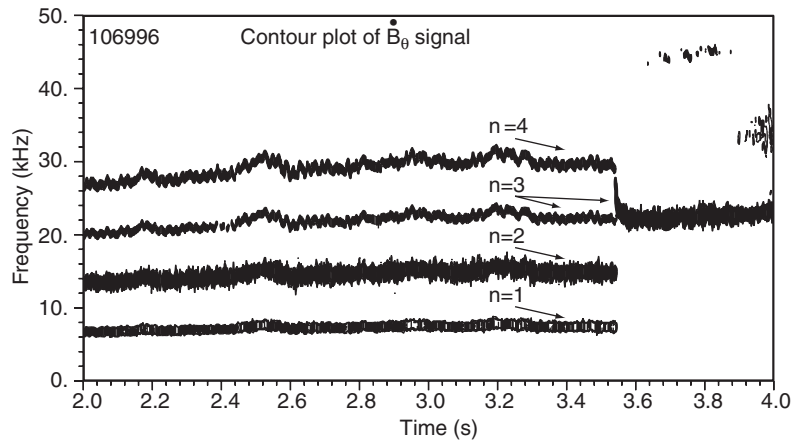


**Figure 7.** Contour plot of the frequency spectrum of a magnetic probe signal from a QDB discharge (106996) as a function of time. The spectrum shows multiple EHO harmonics with toroidal mode numbers  $n = 1-4$ , and time varying harmonic content.

coherent mode result in ELM-free H-mode operation, they are different modes. On DIII-D we have also observed a single example of QDB/QH-mode operation without the EHO, but with a continuous global  $m = 1, n = 1$  mode which extends to the edge. That controlled density, ELM-free H-mode operation can be obtained via a variety of benign MHD activity on a number of machines is encouraging for the robustness and general applicability of these regimes.

In conventional ELM-free H-modes, the density, impurity content, and radiated power all rise monotonically due to the improved particle confinement associated with the edge H-mode transport barrier [18]. In QH-mode plasmas, enhanced particle transport generated by the EHO appears to be responsible for the ability to maintain density and radiated power control in the ELM-free QH-mode regime. Langmuir probe measurements of the ion flux to the divertor strike-points show that the flux is almost entirely carried by the EHO harmonics, i.e. the EHO harmonics account for almost 100% of the ion flux to the probe. In addition, the edge density profile at the outer midplane is directly modulated at the fundamental EHO frequency, as shown in figure 8. These high spatial (sub-cm) and temporal (25  $\mu$ s) resolution measurements were made by an FM profile reflectometer system [19]. Other evidence for increased particle transport associated with the EHO includes an increase in  $D_\alpha$  emission in the entire divertor chamber and a decrease in line density coincident with EHO onset [6].

An important question with regard to the EHO is its location. High-resolution measurements of the density perturbation associated with the EHO, obtained with a profile reflectometer system [19], indicate that the EHO is located at the base of the edge pedestals, at or slightly outside the separatrix, as shown in Figure 9. These data are in good agreement with previous beam emission spectroscopy (BES) [20] results, which also show the EHO perturbation peaking at the separatrix (figure 6 and 7 in [6]).

The modulation of the density profile shown in figure 8 might suggest that the above data could be explained by a different model, one in which the EHO actually resides in the plasma core or in the high gradient pedestal region, generating a movement of the entire edge profile. In this case the BES and reflectometer systems would show a peak density oscillation in the pedestal region (due to the steep density gradients), even though the origin of the EHO was actually further in. Such a model would also be in agreement with conventional MHD mode analysis, which would suggest that the EHO is located in the vicinity of the  $q = 3$  or 4 surfaces. At present we discount this alternative interpretation on the following grounds: as shown by the inset in figure 9(a), the region where the BES and reflectometer systems indicate the EHO peaks is at the base of the edge density pedestal, several cm outside the location of the peak gradients, which occur between densities of  $0.7\text{--}1.5 \times 10^{19} \text{ m}^{-3}$ . If the diagnostics

**Table 1.** Characteristics of edge oscillations in the ELM-free quiescent H-mode on DIII-D and EDA H-mode on C-MOD.

	Edge harmonic oscillation (DIII-D)	Quasi-coherent mode (C-MOD)
Increases $D_\alpha$ level in divertor	Yes	Yes
Increases particle transport across separatrix	Yes	Yes
Location	Foot of edge barrier	Edge density barrier
Frequency	6–10 kHz ( $n = 1$ )	60–200 kHz
Toroidal mode number	Multiple, variable mix $n = 1\text{--}10$	Unknown
Poloidal wavelength	$\sim 100$ cm ( $m \sim 5$ )	$\sim 1$ cm
Edge ion collisionality	Collisionless	Collisional

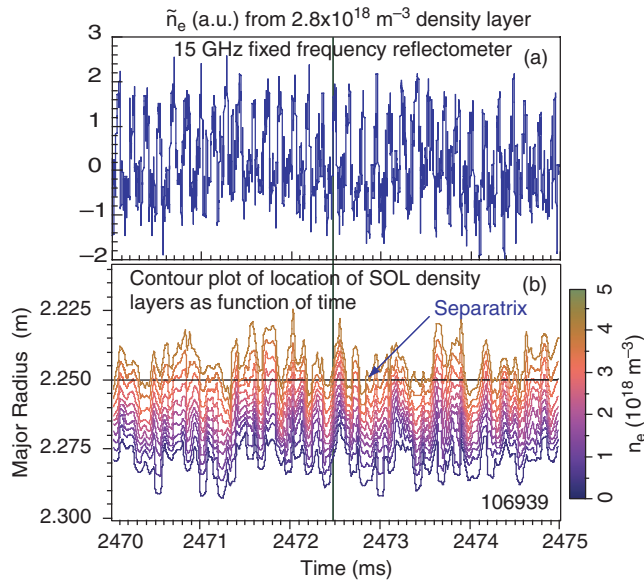


**Figure 8.** For discharge 106939, (a) time history of the signal from a 15 GHz fixed frequency reflectometer, illustrating the EHO oscillation at a density layer of  $2.8 \times 10^{18} \text{ m}^{-3}$ . (b) Colour contour plot of the spatial location of SOL density layers as a function of time, as measured by a profile reflectometer system. By a comparison of (a) and (b) it is apparent that the EHO is modulating the position of the SOL density layers.

were simply responding to a rigid-body motion of the entire profile, then the peak response would be observed further in, in the region of the steepest gradients, which it is not. Other considerations supporting the picture in which the EHO is located at or outside the separatrix were presented in [6], in particular the lack of any mode signatures located in the vicinity of the  $q = 3$  or 4 surfaces. That the EHO does not originate in the high gradient edge pedestal region is also supported by the following consideration. The EHO is known to cause enhanced particle transport, yet the edge pedestal gradients are as steep as in conventional ELMing H-modes, indicating that there is still a particle transport barrier. Consequently, if the EHO were located in the pedestal this would lead to a contradiction. This contradiction is avoided if the EHO resides at the base of the edge pedestal, such that the region of enhanced particle transport is outside the transport barrier.

The EHO has been observed in some low-power co-NBI discharges, but has not resulted in ELM-free operation. Achieving ELM-free operation with an EHO in balanced or co-NBI discharges would significantly extend the operational utility of the QH-mode regime. A goal of the DIII-D program is to achieve a sufficient understanding of the physics of the EHO and QH-mode operation so as to optimize conditions for achieving QH-mode with co-NBI.

### 3.4. ELM stabilization

A fundamental question regarding QH-mode operation is, what is the mechanism that leads to ELM stabilization? We do not have a definitive answer to this question, but can comment on potential mechanisms. One general stabilization mechanism would be a change in the stability boundary. Specific reasons why the stability boundary might change include ion finite Larmor radius (FLR) stabilization effects [15], a change in the edge current density, or  $E \times B$  shear

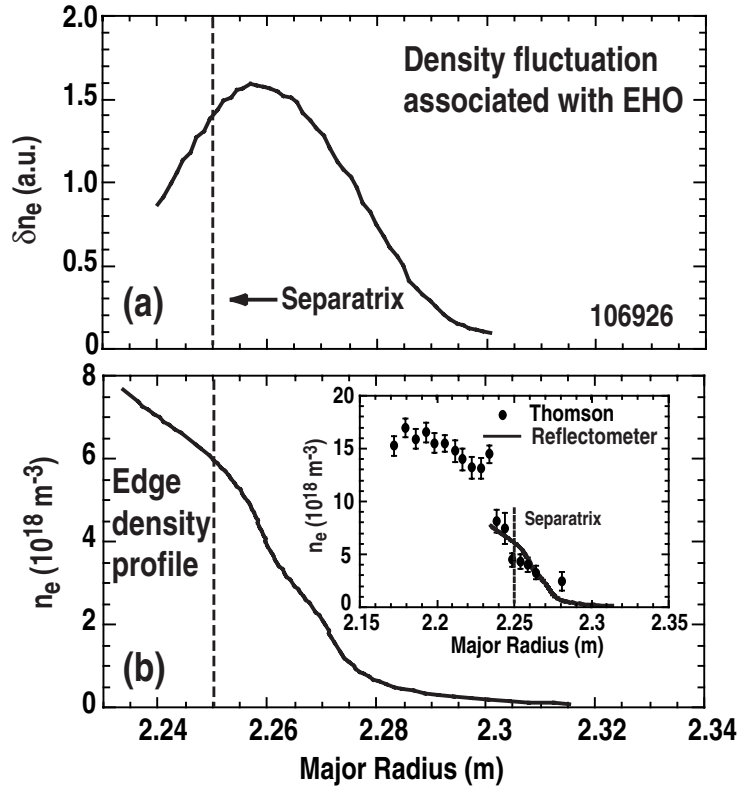


**Figure 9.** Reflectometer profile data relating to the location of the EHO for discharge 106926. (a) Radial profile of the density fluctuations associated with the EHO, as determined from reflectometer data, showing a peak  $\sim 1$  cm outside the separatrix. (b) Edge density profile as measured by the profile reflectometer system, with an inset showing the location of the main plot with respect to the edge pedestal.

effects. With regard to FLR stabilization, it should be noted that the pedestal ion temperatures of 4–7 keV result in larger than usual ion Larmor radii of  $\leq 1.5$  cm, comparable to the width of the edge pedestal. Additional  $E \times B$  shear effects in the QH-mode edge are also likely. As shown and discussed in section 3.2, the edge  $E_r$  well and  $E \times B$  shear are much larger in the QH-mode edge as compared with conventional co-NBI H-modes.

A potential second general reason for ELM stabilization is that the continuous edge MHD may limit the edge pressure gradient, such that the gradient remains below the stability threshold. To first order, this explanation is inconsistent with the observation that the edge  $P_e$  remains the same from the ELMing to the QH-mode phases of individual discharges (section 3.2).

#### 4. Core aspects of QDB operation

In this section we consider core-related aspects of QDB operation, including high-performance operation, transport and fluctuations, and impurity issues.

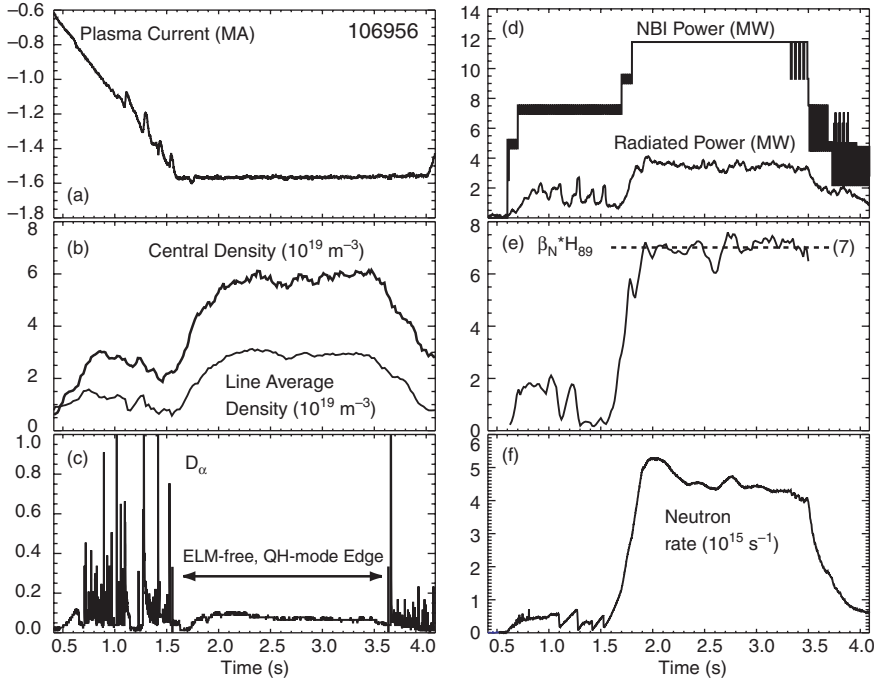


**Figure 10.** Example of the time history of a high-performance QDB plasma (106956), showing (a) plasma current, (b) central and line average electron density, (c) divertor  $D_\alpha$  emission, (d)  $P_{\text{NBI}}$  and total radiated power, (e)  $\beta_N H_{89}$  (the  $H$ -factor is corrected for prompt ion orbit losses), and (f) neutron rate. The period of quiescent QDB/QH-mode operation is marked in (c). This discharge achieves  $\beta_N H_{89} = 7$  for  $10\tau_E$ .

#### 4.1. High performance

High-performance QDB plasmas are created by the addition of core ITBs inside the QH-mode edge. ITB formation is straightforward using standard techniques [8, 14]. Relative performance ( $\beta_N H_{89}$ ) improves with higher input power, while absolute performance ( $\beta_T, S_n$ ) improves with increasing  $I_p$  and  $B_T$ . An example of a high-performance QDB discharge is shown in figure 10. This discharge achieves a constant  $\beta_N H_{89}$  product of 7 for 1.6 s ( $10\tau_E$ ), at  $I_p = -1.6$  MA,  $B_T = 2.0$  T, and  $P_{\text{NBI}} = 11.8$  MW. Other parameters for this discharge include  $T_i(0) = 17$  keV,  $\beta_N = 2.7\%$  mT MA $^{-1}$ ,  $H_{89} = 2.6$ ,  $\beta = 3.8\%$ ,  $W = 1.58$  MJ,  $\tau_E = 160$  ms, and DD neutron rate  $S_n \leq 5.2 \times 10^{15}$  s $^{-1}$ . In this plasma  $q_{\text{min}}$  was  $\sim 1$ ; plasmas with the EHO typically maintain  $q_{\text{min}} > 1$ . Thus, long-pulse high-performance QDB operation has been maintained even with  $q_{\text{min}} \sim 1$  and without sawteeth. The quoted  $H_{89}$  factor and confinement times include a correction for prompt beam ion orbit losses, which is typically of the order of 10%. The discharge was beam fuelled and there is excellent density and radiated power control throughout the high-performance phase, which has a quiescent edge throughout. The high-performance phase in this discharge is limited in duration only by NBI source constraints.

The discharge shown in figure 10 is the only identified example to date where QDB/QH-mode operation was obtained without an EHO. Instead, this discharge has a continuous global  $m = 1, n = 1$  mode, commencing at 1.9 s. The global mode is observed in the edge pedestal by density fluctuation diagnostics, and appears to play the same role as the EHO in other

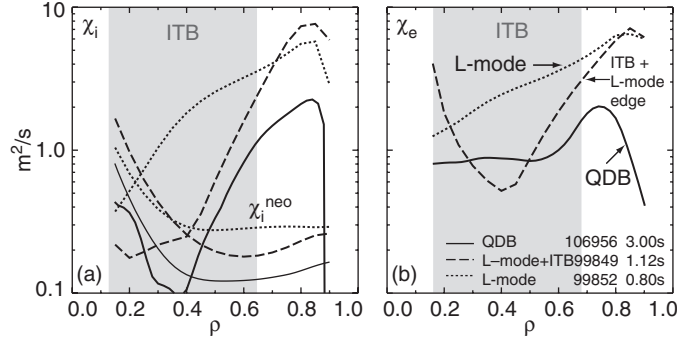


**Figure 11.** Profiles of (a)  $\chi_i$  and  $\chi_i$  neoclassical (thinner lines) and (b)  $\chi_e$ , for three discharges. One is the QDB discharge illustrated in figure 10 (106956, solid curves); the second is a counter injection ITB discharge with an L-mode edge (99849, dashed curves); and the third is an L-mode discharge (99852, dotted curves). Ion thermal diffusivities are reduced to neoclassical levels in the core of the ITB discharges.

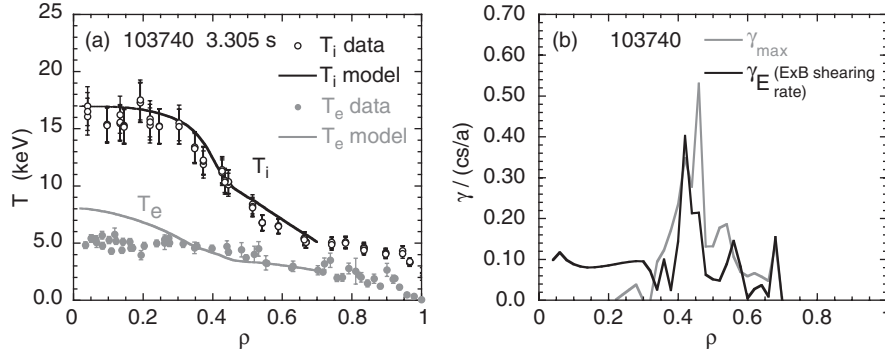


**Figure 12.** GLF23 modelling of QDB discharge 103740. (a) GLF23 steady-state prediction for the ion and electron temperature profiles (black and grey curves, respectively), with a comparison to the actual experimental data (open and filled circles, respectively). (b) Comparison of the maximum calculated turbulence growth rate  $\gamma_{\max}$  (grey curve) to the  $E \times B$  shearing rate  $\gamma_E$  (black curve).

discharges. The beneficial role of this mode is also reminiscent of the benign MHD utilized in other DIII-D controlled density, long-pulse, high-performance discharges [21]. It is important to note that the same level of performance as that shown in figure 10 has been obtained in otherwise identical discharges with the more usual EHO (apart from having higher  $q_{\min}$ , such that the 1/1 mode is not present).

#### 4.2. Core transport and fluctuations

Figure 11 shows transport analysis by the TRANSP code [22], for the same discharge presented in figure 10. To better show the regions of reduced transport, diffusivities are also plotted from a comparable counter-NBI ITB discharge with an L-mode edge, and a standard L-mode discharge. The two (core and edge) regions of reduced transport in the QDB plasma are clearly visible, with core ion thermal diffusivities reduced to neoclassical levels. As discussed in detail in [5], a region of reduced  $E_r$  shear between the edge and core barriers is believed to be responsible for maintaining the separation between the barriers.

Steady-state modelling using the GLF23 gyro-Landau-fluid transport code [23] replicates the core ion transport barrier in these QDB discharges, figure 12(a), though the core electron temperature profile is not accurately predicted. In addition, the GLF23 model shows that the turbulence growth rate and  $E \times B$  shearing rate  $\gamma_E$  are in approximate balance from  $\rho \sim 0.3$  to 0.7, figure 12(b), such that complete turbulence stabilization is not expected in this region, in agreement with separate analysis by the linear gyrokinetic stability (GKS) code [24]. These predictions are in agreement with experimental observations; measurements of low- $k$  turbulence by both FIR scattering and reflectometer systems indicate that core turbulence is not eliminated in these plasmas. In the GLF23 model, the formation of the ion transport barrier is still a consequence of the large  $E \times B$  shear levels regulating the turbulent transport.

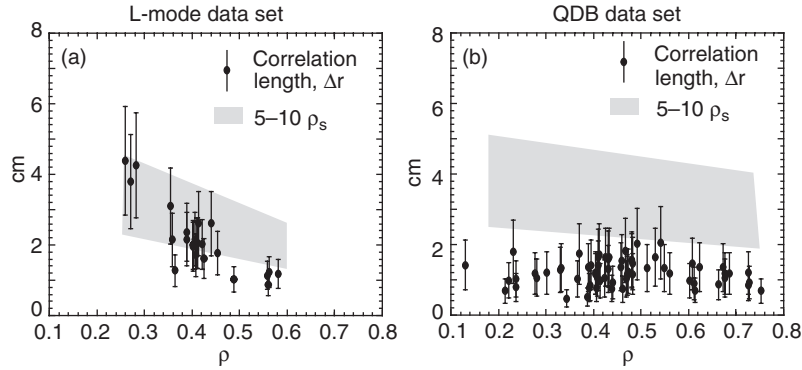


**Figure 13.** Reflectometer measurements of the turbulence radial correlation length  $\Delta r$  (data points with error bars), compared with  $5\text{--}10\rho_s$  (indicated by the shaded regions), for (a) an L-mode data set, and (b) a QDB data set. The correlation lengths are much smaller in the core of QDB plasmas as compared with the scaling observed in L-mode, indicating a reduced step size for turbulent transport.

Reflectometer measurements of the turbulence radial correlation length  $\Delta r$ , shown in figure 13, indicate a substantial reduction in  $\Delta r$  over a measurement range of  $0.1 \leq \rho \leq 0.4$  in QDB plasmas. The reduction is by comparison with previous L-mode measurements [25], in which  $\Delta r$  was found to scale approximately as  $5\text{--}10\rho_s$ . A reduction in the turbulence correlation length should be indicative of a reduction in the step size of the turbulent transport, and occurs in the region of measured transport reduction. This experimental observation of reduced turbulent correlation lengths in QDB plasmas has been replicated by initial non-linear global gyrokinetic modelling of ITG turbulence using the circular-geometry UCAN code [26]. Further modelling is required to verify this result. Thus, initial turbulence modelling of these QDB plasmas shows agreement with experiment with regard to the ion temperature profile and the behaviour of the turbulence amplitude and correlation lengths. That little turbulence amplitude reduction is predicted or seen in regions with neoclassical ion transport will be the subject of further study, via both additional measurements and modelling. Potential mechanisms by which finite turbulence levels can coexist with an ITB are discussed in detail in [27].

#### 4.3. Impurity transport and prospects for steady-state operation

Impurity transport and accumulation is a major issue for long-pulse, high confinement regimes [28]. The constant radiated power in QDB discharges, figures 1 and 10, indicates that the

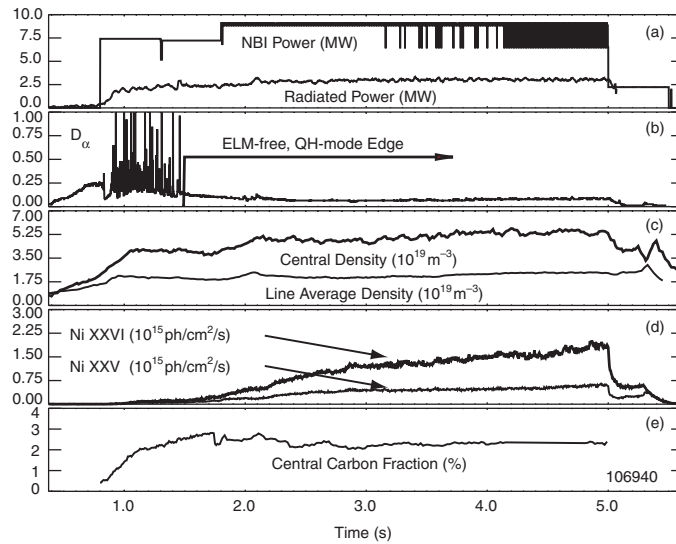


**Figure 14.** Time histories of impurity-related quantities for QDB discharge 106940, showing (a)  $P_{\text{NBI}}$  and total radiated power, (b) divertor  $D_{\alpha}$  emission, (c) central and line average electron density, (d) Ni XXV and XXVI line emission intensities, and (e) central carbon fraction. The central nickel content (Ni XXVI) accumulates with a time constant  $\geq 500$  ms.

edge EHO and global 1/1 mode successfully control the low- $Z$  impurity content as well as the electron density, in strong contrast to the situation with conventional ELM-free H-mode operation [18]. However, high- $Z$  impurities, including nickel, can accumulate during QDB operation, as shown in figure 14. Nickel radiation from the plasma centre continues to increase slowly throughout this QDB discharge, with a time constant  $\geq 500$  ms. However, the central carbon content remains constant, i.e. low- $Z$  impurities (carbon) are not accumulating, but high- $Z$  are. These results are replicated by neoclassical impurity transport modelling, using the STRAHL code [29, 30]. STRAHL predicts both central accumulation of high- $Z$  impurities due to the high-density peaking in these plasmas ( $n_e(0)/\bar{n}_e \sim 2-3$ ), in accord with previous results in other confinement regimes [28], and no preferential carbon accumulation. Spectroscopic analysis and MIST [31] modelling also indicate that for discharge 103818 the nickel had a substantial impact on the total  $Z_{\text{eff}}$ ; without high- $Z$  impurities the total  $Z_{\text{eff}}$  would have been  $\sim 2.4$ , as opposed to the actual total  $Z_{\text{eff}}$  of  $\sim 4.1$ .

TRANSP [22] analysis indicates that the neutron rate in QDB plasmas is reduced by  $\sim 40-70\%$  compared with what would be obtained if the nickel were absent. This implies that QDB fusion performance could be substantially improved if the high- $Z$  impurities were reduced. That the measured total radiated power remains constant while the nickel accumulates is explained by the fact that the total power radiated by the nickel is small,  $< 300$  kW. The slow central high- $Z$  accumulation also leads to the rise in central electron density visible in figure 14(c), and also visible in figures 1 and 10.

Experiments have been performed to directly measure high- $Z$  impurity transport rates in QDB discharges in order to determine if the nickel accumulation is due to source or transport effects, and results will be available later in 2001. There is evidence in QDB discharges of enhanced plasma-wall interactions, which may provide a strong impurity source. If such a source cannot be confirmed or eliminated, then an alternative solution would be to actively reduce the density peaking. The density peaking has been reduced transiently in QDB plasmas

using a variety of techniques, including increasing the plasma triangularity [6], edge impurity injection, and off-axis pellet injection.

As discussed in [5], reducing the density peaking would also have the benefit of improving bootstrap current alignment; QDB plasmas have a bootstrap fraction of up to 45% , but peaked on-axis. In addition, NBCD from counter-NBI generates 10–15% of the total current, but in the opposite direction. Modelling work has been initiated to explore the fully non-inductive, steady-state potential of the QDB regime. Initial conclusions are that the lower densities and higher electron temperatures in QDB plasmas are highly favourable for off-axis ECCD. As might be expected, however, additional on-axis current drive is required to control  $q_0$  in the presence of the significant counter-NBCD. Simulations over 10 s with no Ohmic current and using 3 MW of FW for on-axis current drive and 6 MW of off-axis ECCD indicate potential for control of the  $q$  profile.

## 5. Conclusions

The results reported here demonstrate that sustained, high-performance ELM-free H-mode plasmas are possible with good density and radiated power control. The results also demonstrate that the quiescent, ELM-free edge can easily be combined with core ITBs so as to obtain the benefits of both core and edge transport barriers. The combination of core ITBs and edge H-mode temperature pedestals in the new QDB regime results in high-performance plasmas; a  $\beta_N H_{89}$  product of 7 has been maintained for  $10\tau_E$ . The double barriers have been maintained for  $>3.5$  s ( $\sim 25\tau_E$ ), demonstrating a long-pulse, quasi-steady-state capability. Substantial progress has been made in understanding the processes leading to the creation of the quiescent H-mode edge and characterizing the benign MHD activity associated with QH-mode operation. In the plasma core, transport and turbulence measurements are in agreement with initial modelling and simulation results, though more comparisons are required.

## Acknowledgments

This is a report of work supported by the US Department of Energy under Grant Nos DE-FG03-01ER54615, DE-FG02-89ER53297, DE-FG02-92ER54141, DE-FG03-96ER54373, DE-FG03-95ER54294, DE-FG02-90ER54084, and Contract Nos DE-AC03-99ER54463, DE-AC05-00OR22725, W-7405-ENG-48, DE-AC02-76CH03073 and DE-AC04-94AL85000.

## References

- [1] ITER Physics Basis Document 1999 *Nucl. Fusion* **39** 2137
- [2] Leonard A W *et al* 1999 *J. Nucl. Mater.* **266–269** 109
- [3] Lao L L *et al* 2000 *Plasma Phys. Control. Fusion* **42** A51
- [4] Doyle E J *et al* 2001 Progress towards increased understanding and control of internal transport barriers on DIII-D *Proc. 18th IAEA Fusion Energy Conf. (Sorrento, 2000)* (Vienna: International Atomic Energy Agency) *Nucl. Fusion* at press
- [5] Greenfield C M *et al* 2001 *Phys. Rev. Lett.* **86** 4544
- [6] Burrell K H *et al* 2001 *Phys. Plasmas* **8** 2153
- [7] Yushmanov P N *et al* 1990 *Nucl. Fusion* **30** 1999
- [8] Greenfield C M *et al* 2000 *Phys. Plasmas* **7** 1959
- [9] Rice B W *et al* 1999 *Nucl. Fusion* **39** 1855
- [10] Strait E J *et al* 1997 *Phys. Plasmas* **4** 1783
- [11] Fujita T *et al* 1999 *Nucl. Fusion* **39** 1627
- [12] Kamada Y *et al* 1999 *Nucl. Fusion* **39** 1845
- [13] Söldner F X *et al* 1999 *Nucl. Fusion* **39** 407

- 
- [14] Rice B W *et al* 1996 *Nucl. Fusion* **36** 1271  
Rice B W *et al* 1996 *Phys. Plasmas* **3** 1983
  - [15] Ferron J R *et al* 2000 *Phys. Plasmas* **7** 1976
  - [16] Hinton F L and Kim Y-B 1995 *Phys. Plasmas* **2**, 159
  - [17] Hubbard A *et al* 2001 *Phys. Plasmas* **8** 2033
  - [18] Jackson G J *et al* 1992 *Phys. Fluids B* **4** 2181
  - [19] Zeng L *et al* 2001 *Rev. Sci. Instrum* **72** 320
  - [20] McKee G R *et al* 1999 *Rev. Sci. Instrum* **70** 913
  - [21] Wade M R *et al* 2001 *Phys. Plasmas* **8** 2208
  - [22] Hawryluk R J 1980 *Proc. of the Course in Physics Close to Thermonuclear Conditions (Varena, 1979)* vol I (Brussels: CEC) p 19
  - [23] Waltz R E *et al* 1997 *Phys. Plasmas* **4** 2482
  - [24] Waltz R E *et al* 1999 *Phys. Plasmas* **6** 4265
  - [25] Rhodes T L *et al* 2000 *Proc. 27th EPS Conf. on Controlled Fusion and Plasma Physics*, ECA vol 24B (Budapest, Hungary, 2000) p 564
  - [26] Sydora R D *et al* 1996 *Plasma Phys. Control. Fusion* **38** A281
  - [27] Doyle E J *et al* 2000 *Plasma Phys. Control. Fusion* **42** A237
  - [28] Baker D R *et al* 2001 *Phys. Plasmas* **8** 1565
  - [29] Behringer K 1987 Description of the impurity transport code STRAHL JET-R(87)-08, JET Joint Undertaking, Culham, UK
  - [30] Peeters A G 2000 *Phys. Plasmas* **7** 268
  - [31] Hulse R A 1983 *Nucl. Technologies/Fusion* **3** 259